IJASS
International Journal of
Aeronautical and Space Sciences

Numerical Study about Aerodynamic Interaction for Coaxial Rotor Blades

Sang Hyun Park[1] · Oh Joon Kwon[1]

Abstract

In the present study, the interaction effect by inter-rotor spacing of coaxial rotor blades in hovering and forward flight is studied by using a Reynolds-averaged Navier–Stokes CFD flow solver based on mixed meshes. The meshes were composed of unstructured near-body region and Cartesian off-body region. The flux-difference splitting scheme of Roe was used for computing inviscid fluxes on the near-body region, whereas the 7th order WENO scheme was used for the computation of the inviscid fluxes on the off-body region to capture vortex with high resolution. The predicted results of the baseline inter-rotor spacing were compared with the reference results of other researchers for validation. The computed results of three different inter-rotor spacings were compared in terms of the thrust and torque coefficients for each flight condition. The cause of the different interaction effect by inter-rotor spacing between hovering and forward flight was also investigated.

Keywords Coaxial rotor · Inter-rotor spacing · Mixed mesh flow solver

1 Introduction

Conventional helicopters are known to have the limitation of maximum cruise speed in forward flight due to the structural and aerodynamic characteristics of the rotorcraft. In order to overcome this limitation, rotorcrafts using alternative propulsion system have been developed for several decades. Among various types of propulsion system, coaxial rotor has been receiving attention due to high stability and compactness. For these reasons, coaxial rotors, including Harrington rotor [1], Nagashima rotor [2], and XV-15 rotor [3], were developed and experimented for the several decades. However, the mechanical complexity of the coaxial rotor hub to derive rotors in opposite direction is revealed to be prone to the loss of the aerodynamic performance and even failures. Later with the development of the Sikorsky X2 rotorcraft, which solved the structural problem of the coaxial rotor hub, coaxial rotor system has been widely adapted for various rotorcrafts again.

Unlike other conventional rotorcrafts, inter-rotor spacing (IRS) is considered to be a unique design parameter of the coaxial rotorcraft which affects the aerodynamic performance. As a result, the effect of IRS on the aerodynamic performance of the XV-15 coaxial rotor in hovering flight was recently investigated in [3, 4]. In the present study, the numerical computations of Nagashima coaxial rotor in hovering flight and Harrington rotor 1 in forward flight were carried out by changing IRS from the baseline. A three-dimensional flow solver based on Cartesian/unstructured mixed meshes was used for the computation. An overset mesh technique was adopted to effectively describe the relative motion of the coaxial rotor. The validation of the flow solver was carried out by comparing the computational results with the reference data of the baseline IRS. The effect of IRS on the coaxial rotor was studied by comparing the vortex structure, downwash and aerodynamic coefficients of three different IRS under each flight conditions.

2 Numerical Method

The three-dimensional, compressible Reynolds-averaged Navier–Stokes equations were used for the computation of the coaxial rotors. The governing equations can be written

✉ Oh Joon Kwon
ojkwon@kaist.ac.kr

1 Department of Aerospace Engineering, Korea Advanced Institute of Science and Technology, Daejeon 34141, Republic of Korea

in an integral form for an arbitrary computational domain V with boundary δV as follows:

$$\iiint_V \frac{\partial}{\partial t}\vec{Q}\mathrm{d}V + \oint_{\partial V}(\vec{F}(\vec{Q})\cdot\vec{n})\mathrm{d}S = \oint_{\partial V}(\vec{G}(\vec{Q})\cdot\vec{n})\mathrm{d}S. \qquad (1)$$

$\vec{Q}$ in Eq. 1 indicates the vector of the conservative variables for mass, momentum, and energy equations, whereas $\vec{n}$ denotes the outward normal vector on the control surface. $\vec{F}(\vec{Q})$ and $\vec{G}(\vec{Q})$ indicate the inviscid and viscous fluxes.

The meshes were composed of unstructured near-body region and Cartesian off-body region. The governing equations were discretized using vertex and cell-centered finite volume methods in the near-body and off-body region, respectively. Modified central difference scheme is used for computing diffusion terms in both regions. Implicit time integration is used for advancing solutions in time with 20 times of dual-time stepping.

2.1 Near-Body Flow Solver

The unstructured tetrahedral and prismatic meshes were adopted for the spatial discretization in the near-body region. The unstructured meshes offer the largest flexibility in the treatment of complex geometries while ensuring proper resolution of the boundary layer region by adopting prismatic elements near solid walls at the same time. By applying the vertex-centered scheme, the flow domain is divided into a finite number of control volumes composed of median dual cells surrounding each vertex. The convective fluxes are computed by employing the flux-difference splitting scheme of Roe. Second-order spatial accuracy of the flow variables is achieved by using a linear reconstruction at each faces of the cell. The diffusive fluxes are computed by adopting a modified central differencing scheme. The Spalart–Allmaras one-equation turbulence model is adopted to solve transport equation for a turbulent eddy-viscosity variable. The rotation-curvature correction was used in the turbulence model in order to resolve the tip vortices better. Venkatakrishnan slope limiter was also used for enhancing the stability of the numerical computation.

2.2 Off-Body Flow Solver

The off-body region is divided into the unstructured Cartesian meshes. The 7th order WENO scheme is adopted for computing the fluxes, achieving high order of accuracy in space. Since the octree technique is utilized for the generation of the meshes at off-body region, the Cartesian meshes contain hanging nodes and the solution of high order accuracy could be polluted by a sudden change of the cell size at these hanging nodes. To minimize the error caused at the

hanging nodes, multidimensional interpolations are adopted for the computation [5].

2.3 Overset Mesh Technique and Parallel Implementation

An overset mesh technique is adopted to interpolate the flow variables between near-body and off-body regions [7]. Adopting overset mesh technique made it possible to handle relative motion of counter-rotating coaxial rotor blades, as well as connecting different types of mesh systems. The overset mesh technique is composed of searching, hole-cutting, and interpolation procedures. In the present mixed mesh flow solver, neighbor-to-neighbor (N2N) search technique was implemented to conduct searching process fast with robustness. With the introduction of the linear shape functions, second-order accuracy of the interpolation was achieved, resulting in accurate exchange of the flow variable information.

A parallel computational algorithm based on a domain decomposition strategy is adopted to reduce the large computational time to handle a large number of cells. The load balancing between processors is achieved by partitioning the global computational domain into local subdomains using the MeTiS libraries. The Message Passing Interface is used to transfer the flow variables across the subdomain boundary.

2.4 Hovering Flight Condition

Nagashima coaxial rotor is used for the hovering flight computation. Geometry and flight condition of the Nagashima rotor are given in Fig. 1 and Table 1. Detailed information about meshes used for the calculation is given in Table 2. The IRS is set to 0.1, 0.2, and 0.4 for the comparison.

2.5 Forward Flight Condition

Harrington rotor 1 is used for the calculation of the coaxial rotor in forward flight. The geometry and the flight condition of the Harrington rotor 1 [8] are shown in Fig. 2 and Table 3. Trim condition for the Harrington rotor 1 in forward flight, which is computed with CAMRAD II [8], is also given in Table 4. Similar number of grid points is used for the computation of Harrington rotor 1 compared with those used for
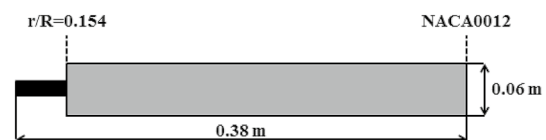

Fig. 1 Nagashima rotor blade model

Table 1 Geometry and flight condition of Nagashima rotor

Criteria	Specification
Radius	0.38 m
Chord Length	0.06 m
Blade Section	NACA0012
Root-cut	15.4%
IRS (H/D)	0.2
Solidity	0.1
α_{upper}	9°
α_{lower}	10°
Tip Mach Number	0.37
Reynolds Number	0.38×10^6

Table 2 Number of nodes used for computation

No. of nodes	Near-body (per blade)	Off-body	Total
Nagashima rotor	1.89×10^6	6.61×10^6	1.42×10^7
Harrington Rotor 1	1.77×10^6	9.27×10^6	1.64×10^7
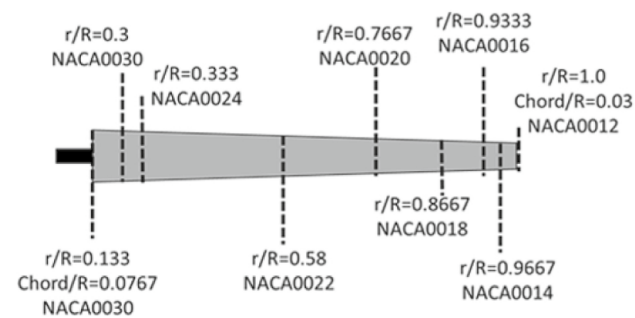
Fig. 2 Harrington rotor 1 blade model [8]

Table 3 Flight condition of Harrington rotor 1

Criteria	Specification
IRS	0.19
Tip Mach Number	0.4169
Reynolds Number	1.1×10^6
Advance Ratio	0.2

Table 4 Trim condition of Harrington rotor 1

Criteria	Upper rotor	Lower rotor
αs	− 5.47°	− 5.47°
θ	9.21°	9.19°
θ_{1S}	− 4.57°	− 4.36°
θ_{1C}	0.50°	0.63°

the Nagashima rotor to eliminate any difference caused by the difference of the grid number and investigate how IRS impacts on the aerodynamic performance of the coaxial rotor depending on the flight condition. The IRS is set to 0.19, 0.38, and 0.57 for the comparison (Fig. 3).

3 Results and Discussion

The computational results of the baseline IRS are compared with the experimental results and computational results of other researchers for validation. Then the aerodynamic interaction effect of the coaxial rotor in hovering flight and forward flight is studied by changing IRS with each flight conditions.

3.1 Nagashima Rotor in Hovering Flight

Three different IRS, 0.1, 0.2, and 0.4, are selected and compared with Nagashima rotor in hovering flight condition. The baseline results indicate the results of IRS 0.2, which is the IRS used in the experiment. Experimental thrust coefficient of the Nagashima rotor is given to be 0.00981 in [2], whereas the computational result gives 0.00974, showing about 0.7% error.

In Fig. 4, vortex structure of the Nagashima rotor is shown by different IRS. Iso-surface of the 0.1 vorticity is shown with the q-criterion contour in the range from -0.01 to 0.005. The vortex starts to break down after about 720° when IRS is 0.4, however, the effect of IRS on the overall structure of the vortex could hardly be found in hovering flight.

Sliced view of the vorticity from Fig. 4 is shown in Fig. 5. The contour level is set from 0 to 0.15. From the figure, the strength of the BVI gets weaker as IRS gets larger due to dissipation. The location of the BVI also moves towards inside of the lower rotor blade.

Thrust coefficient by azimuth angle is shown in Fig. 6. Each of the red, blue, and green line denotes the results of 0.1, 0.2, and 0.4 IRS. Both thrust coefficients of upper and lower blade show periodic behavior by the characteristic of the coaxial rotor in hovering flight. This periodicity occurs 4 times per revolution. As IRS gets larger, the interaction effect between the upper and lower rotor gets weaker, resulting in smaller amplitude of fluctuation at the thrust coefficient graphs. In addition, the amplitude of the secondary fluctuation which occurs near the azimuth angle of 90°, 180°, 270° and 360° gets smaller as the interaction effect between upper and rotor rotors gets weaker with larger IRS.

The averaged values of the thrust coefficients per revolution are given in Table 5. The given total thrust coefficient values are calculated by summing the values of the averaged thrust coefficients. The thrust coefficient of the
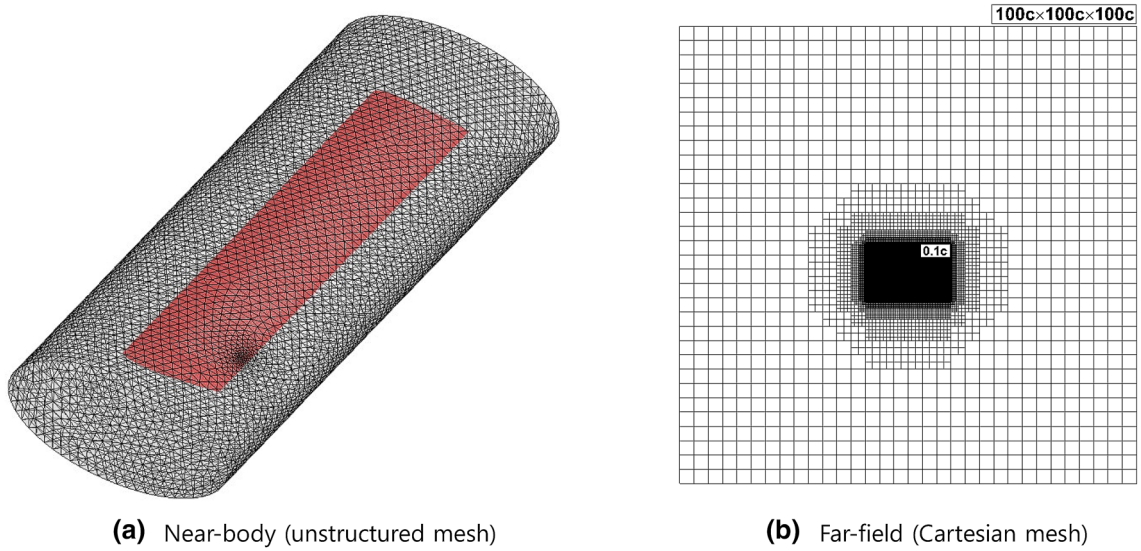
(a) Near-body (unstructured mesh)   **(b)** Far-field (Cartesian mesh)

Fig. 3 Grid system used for the mixed mesh flow solver (Nagashima rotor)

(a) IRS = 0.1   **(b)** IRS = 0.2   **(c)** IRS = 0.4
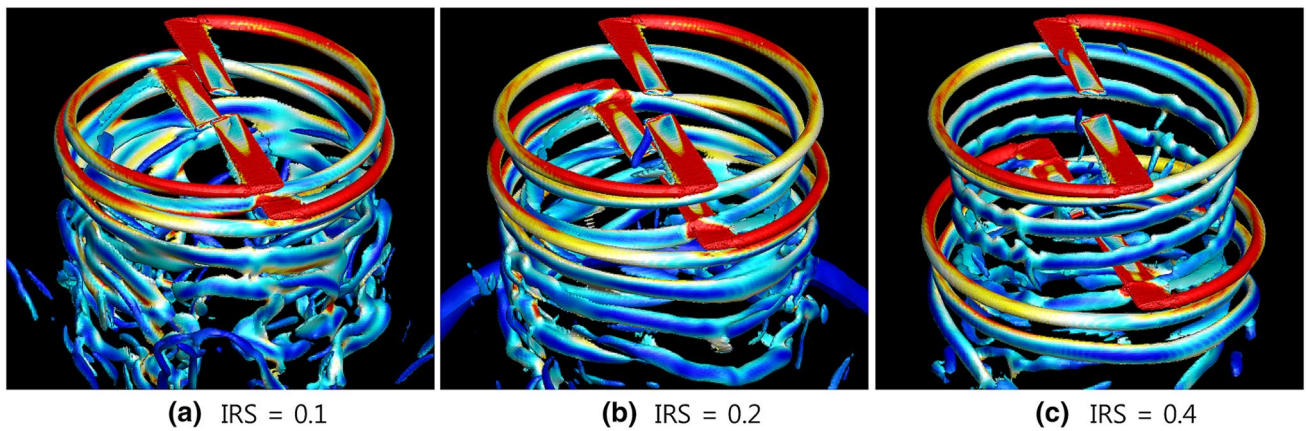
Fig. 4 Vortex structure of Nagashima rotor by IRS

(a) IRS = 0.1   **(b)** IRS = 0.2   **(c)** IRS = 0.4
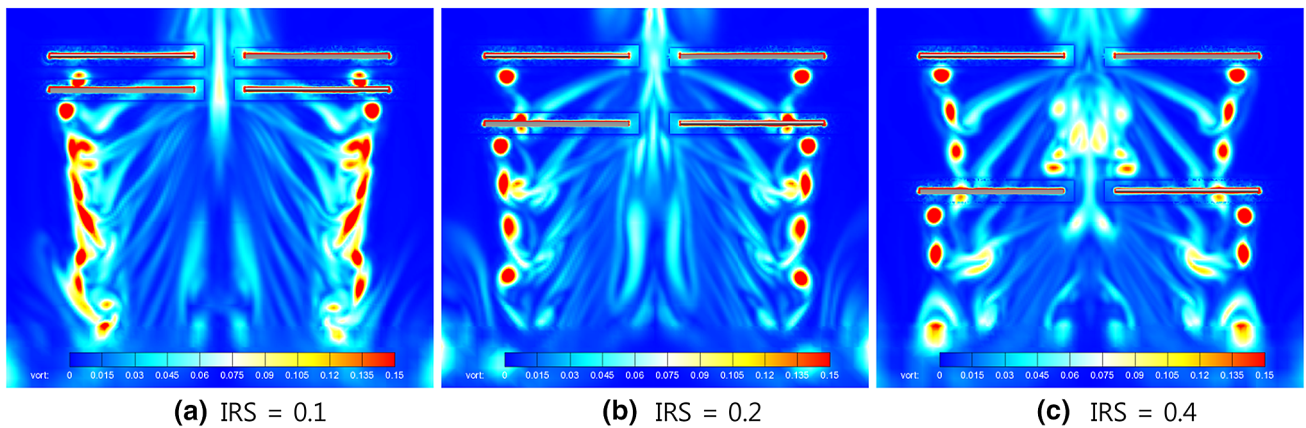
Fig. 5 Vorticity contour of Nagashima rotor by IRS

(a) Upper rotor   **(b)** Lower rotor

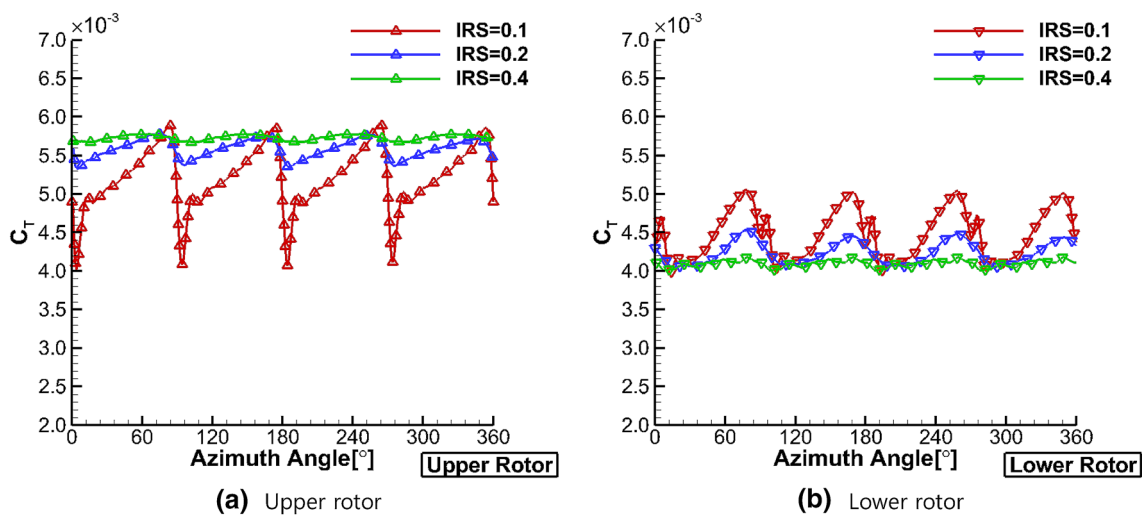**Fig. 6** Thrust coefficients of the Nagashima rotor by azimuth angle

Table 5 Averaged thrust coefficients of Nagashima rotor

	IRS = 0.1	IRS = 0.2	IRS = 0.4
$C_{T,\text{Upper}}$	5.25×10^{-3}	5.59×10^{-3}	5.75×10^{-3}
$C_{T,\text{Lower}}$	4.48×10^{-3}	4.04×10^{-3}	3.81×10^{-3}
$C_{T,Total}$	9.74×10^{-3}	9.63×10^{-3}	9.56×10^{-3}
Ref.C_T	–	9.81×10^{-3}	–

Table 6 Averaged torque coefficients of Nagashima rotor

	IRS = 0.1	IRS = 0.2	IRS = 0.4
$C_{Q,\text{Upper}}$	9.99×10^{-4}	1.02×10^{-3}	1.03×10^{-3}
$C_{Q,\text{Lower}}$	1.02×10^{-3}	9.90×10^{-4}	9.69×10^{-4}
$C_{Q,\text{Total}}$	2.94×10^{-5}	2.89×10^{-5}	5.80×10^{-5}
$abs(C_{Q,\text{Total}})$	2.02×10^{-3}	2.01×10^{-3}	2.00×10^{-3}

upper rotor gets larger with larger IRS, whereas that of the lower rotor gets smaller. Since the loss of the thrust coefficient from lower rotor is higher than the gain of that from upper rotor, the total thrust coefficient decreases with the increment of IRS in the hovering flight. This result follows with the reported trend of the XV-15 coaxial rotor in [3, 4].

In Table 6, averaged torque coefficients of the Nagashima rotor per revolution are shown. $C_{Q,Total}$ indicates the total torque coefficient generated by the rotor, whereas abs($C_{Q,\text{Total}}$) represents the total torque coefficient needed to derive the rotor. Since the collective pitch for the baseline given in Table 1 represents the torque-balanced angle, $C_{Q,Total}$ is minimized when IRS is 0.2. On the other hand, $abs(C_{Q,Total})$ decreases as IRS increases, showing similar trend compared to the thrust coefficient results.

3.2 Harrington Rotor 1 in Forward Flight

Three different IRS, 0.19, 0.38, and 0.57, are selected and compared for Harrington rotor 1 in forward flight. The baseline results denote the results of IRS 0.19, which are the computational results with CAMRAD II given in [8]. The reference thrust coefficient is given to be 0.0048, whereas the present computational result gives 0.0054.

Vortex structure of the Harrington rotor 1 by different IRS is given in Fig. 7. Iso-surface of the 0.03 vorticity is shown with the q-criterion contour in the range from -0.006 to 0.001. As IRS gets smaller, the trailing vortex from the upper and lower rotors merges together and forms a complicated vortex structure.

The sliced view of the vorticity from Fig. 7 is shown in Fig. 8. The contour level is set from 0 to 0.05. The strength of the BVI gets weaker with larger IRS due to dissipation, which is the same trend shown with Nagashima rotor in hover. Furthermore, BVI location falls backward on the lower rotor as IRS increases, and it eventually disappears with the IRS over 0.57.

Thrust coefficient by azimuth angle is drawn in Fig. 9. Each of the red, blue, and green line indicates the results of 0.19, 0.38, and 0.57 IRS. Both thrust coefficients of the upper and lower blade show the periodic characteristic in forward flight. The dominant periodicity is shown to be 2 times per revolution, whereas secondary periodicity occurs 4 times per revolution. The former periodicity is caused by the characteristic behavior of the rotor in forward flight, whereas the latter periodicity is caused by the interaction effect between the upper and lower rotor of the coaxial rotor. The interaction effect between upper and lower rotor gets weaker with larger IRS, resulting in smaller amplitude of the secondary fluctuation in the thrust coefficient graphs.
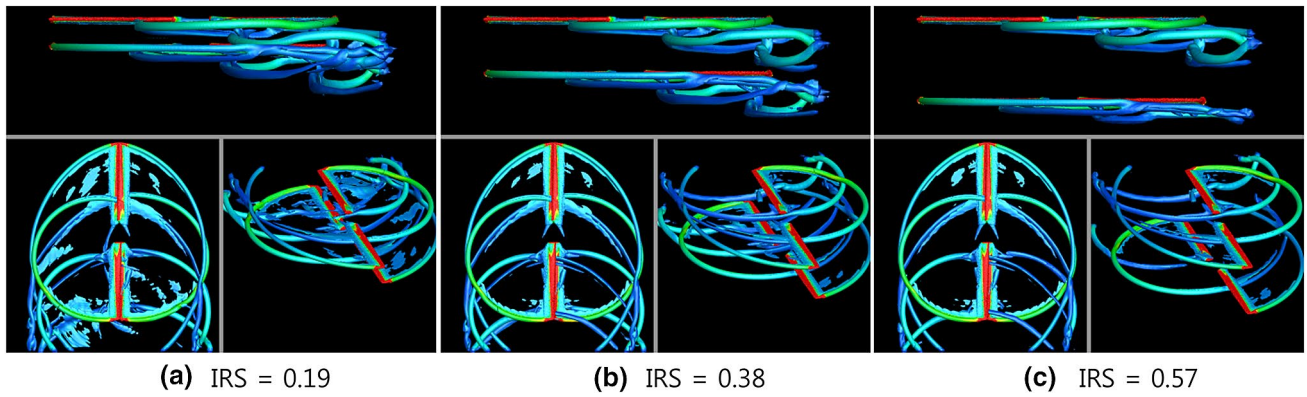
(a) IRS = 0.19   **(b)** IRS = 0.38   **(c)** IRS = 0.57

Fig. 7 Vortex structure of Harrington rotor 1 by IRS

(a) IRS = 0.19   **(b)** IRS = 0.38   **(c)** IRS = 0.57
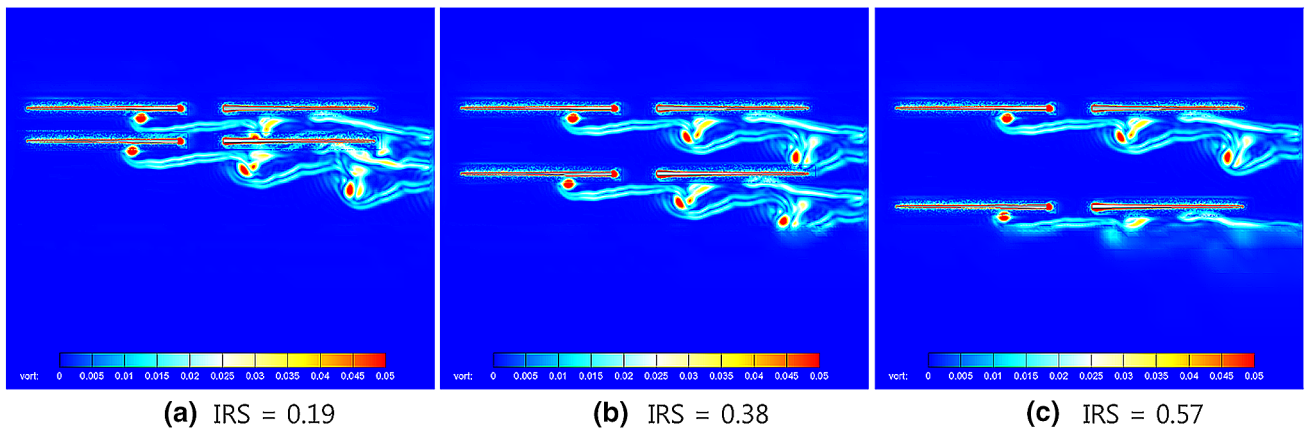
Fig. 8 Vorticity contour of Harrington rotor 1 by IRS
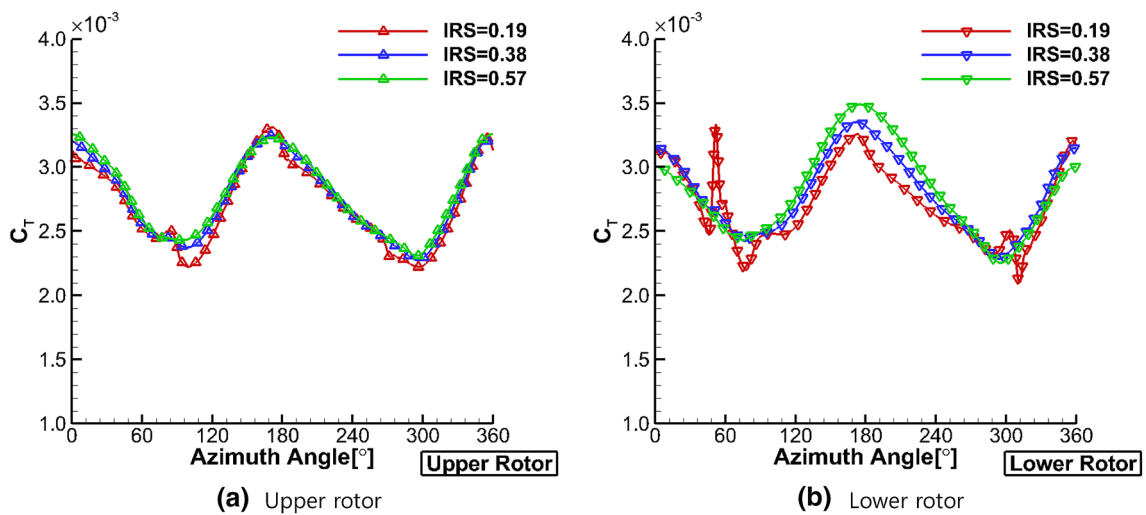

(a) Upper rotor   **(b)** Lower rotor

Fig. 9 Thrust coefficients of the Harrington rotor 1 by azimuth angle

Table 7 Averaged thrust coefficients of Harrington rotor 1

	IRS = 0.19	IRS = 0.38	IRS = 0.57
$C_{T,Upper}$	2.71×10^{-3}	2.75×10^{-3}	2.79×10^{-3}
$C_{T,Lower}$	2.72×10^{-3}	2.79×10^{-3}	2.82×10^{-3}
$C_{T,Total}$	5.42×10^{-3}	5.55×10^{-3}	5.60×10^{-3}
$Ref.C_T$	4.80×10^{-3}	-	-

Table 8 Averaged torque coefficients of Harrington rotor 1

	IRS = 0.19	IRS = 0.38	IRS = 0.57
$C_{Q,Upper}$	3.24×10^{-4}	3.25×10^{-4}	3.25×10^{-4}
$C_{Q,Lower}$	3.23×10^{-4}	3.24×10^{-4}	3.25×10^{-4}
$C_{Q,Total}$	4.96×10^{-7}	2.48×10^{-7}	7.15×10^{-7}
$abs(C_{Q,Total})$	6.47×10^{-4}	6.49×10^{-4}	6.51×10^{-4}

The overall thrust coefficient of the lower rotor is shown to be affected more by the change of the IRS compared to that of the upper rotor.

The averaged values of the thrust coefficients per revolution are given in Table 7. The given values are calculated in the same manner as Nagashima rotor. For the Harrington rotor 1 in forward flight, both upper and lower rotor thrust coefficients increase as IRS gets larger. As a result, the total thrust coefficients increases with larger IRS.

In Table 8, averaged torque coefficients of the Harrington rotor 1 per revolution is given. Same calculation methods used for the computation of the torque coefficients with Nagashima rotor are adopted as well. The torque coefficients are not much affected by the change of the IRS compared to the Nagashima rotor. The summed absolute values of torque

coefficients increase with larger IRS, showing opposite trend from hovering flight condition. This result also follows with the trend found in thrust coefficient of the Harrington rotor 1 at the same time.

3.3 Difference in Thrust Coefficient of Hover and Forward Flight

The effect of IRS on the aerodynamic coefficients of the coaxial rotor is studied with Nagashima rotor in hovering flight and Harrington rotor 1 in forward flight. For the hovering flight, total thrust coefficient decreases as IRS increases. This trend follows the result suggested from the references [3, 4]. For the forward flight, however, total thrust coefficient increases with larger IRS, and this trend is generally thought to be the aerodynamic characteristic of the coaxial rotor.

Thrust coefficients of Nagashima rotor and Harrington rotor are compared in Fig. 10. Each of the red upper triangle symbolled line, blue lower triangle symbolled line, and green diamond symbolled line represents the thrust coefficient of the upper, lower, and total rotor. Thrust coefficients of both Nagashima and Harrington rotor 1 at upper rotor increase with larger IRS. However, the main difference is found at the thrust coefficient of lower rotor. As IRS gets larger, thrust coefficient at the lower rotor of Nagashima rotor decreases, whereas that of Harrington rotor 1 increase, resulting in opposite trend of total thrust coefficient.

Downwash at the lower rotor of each coaxial rotor viewed from above is compared in Figs. 11 and 12 to find out the cause of this difference. Since the flight condition is different, the contour levels are fitted for each rotor for the comparison. Contour level from − 0.07 to 0 is set for Nagashima rotor, whereas contour level from − 0.03 to − 0.01 is set for
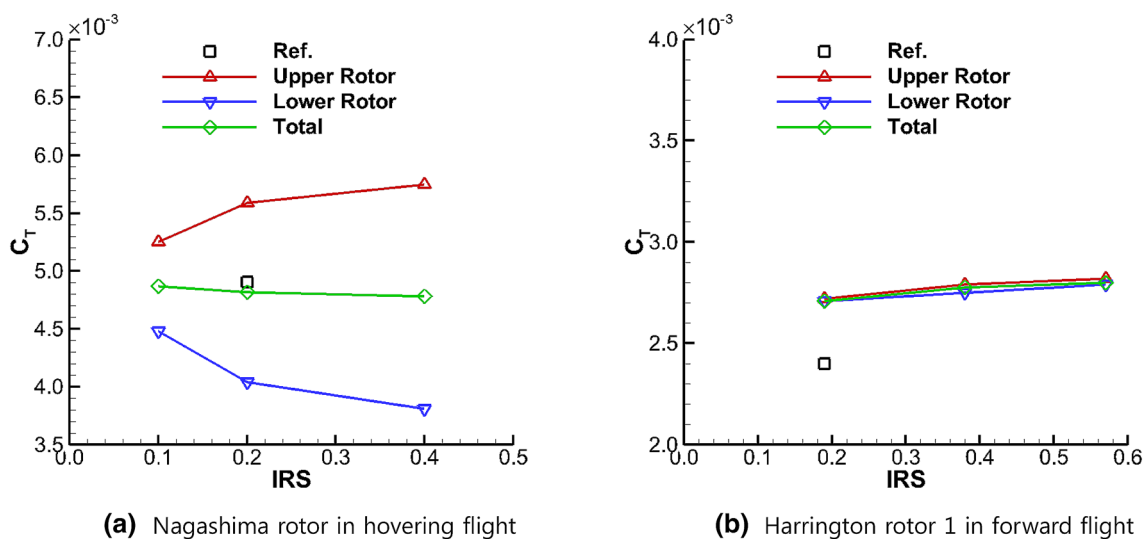

(a) Nagashima rotor in hovering flight

(b) Harrington rotor 1 in forward flight

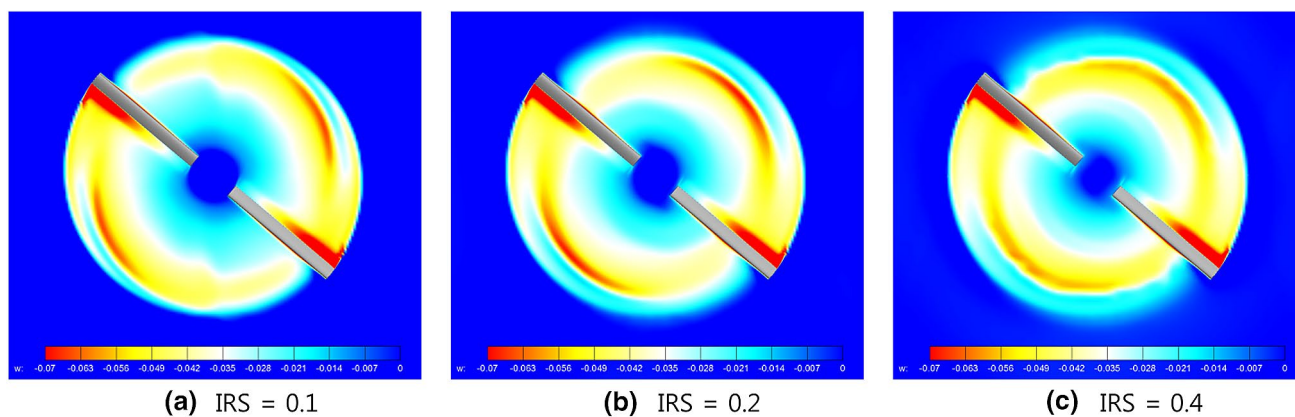**Fig. 10** Average thrust coefficient by IRS

Fig. 11 Downwash at lower rotor of Nagashima rotor viewed from above
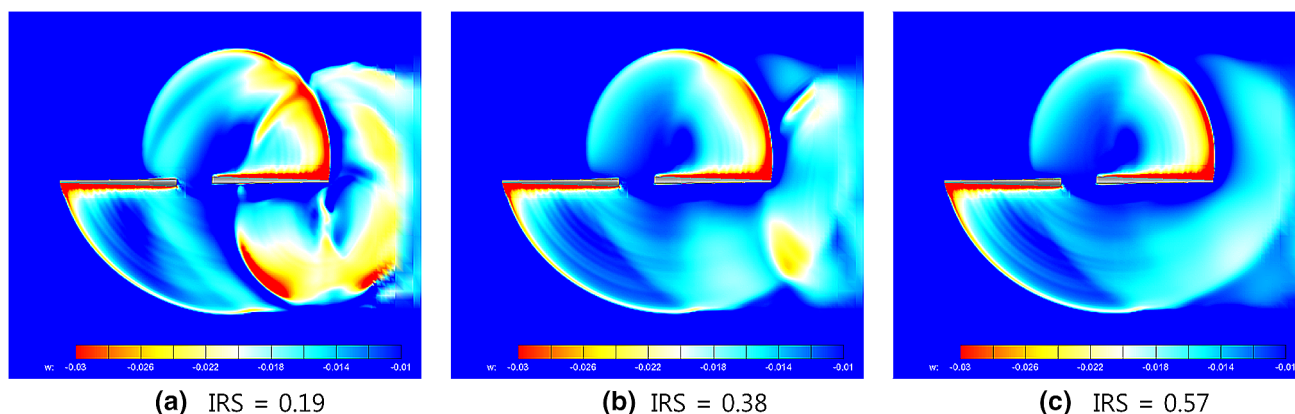

Fig. 12 Downwash at lower rotor of Harrington rotor 1 viewed from above

Harrington rotor 1. The interaction of the upper and lower rotor is generally thought to be weakened with larger IRS, if the aerodynamic characteristics of the upper rotor do not change. Moreover, it can be suggested that the region at lower rotor affected by the upper rotor also decreases with larger IRS from Fig. 0.9. As a result, the strength of the downwash at the lower rotor in forward flight decreases with larger IRS, as shown in Fig. 12.

On the contrary, downwash strength at the lower rotor of Nagashima rotor increases as IRS gets larger. From Fig. 11, it is shown that the downwash strength gets stronger and impacts more to the inboard of the lower rotor as IRS gets larger. The cause of this phenomenon can be found in Figs. 13 and 14.

In Fig. 14, the downwash of the upper rotor is almost developed fully in forward flight condition even with smaller IRS, and it does not vary much as IRS changes. Since the downwash gets weaker by dissipation with larger IRS, the downwash strength at the lower rotor of the Harrington rotor 1 decreases. The decrease in the strength of the downwash makes an increase in the effective angle of attack at the lower

rotor. As a result, the thrust coefficient of the lower rotor in forward flight increases as IRS increases.

In Fig. 13 on the other hand, the downwash of the upper rotor is not fully developed with 0.1 IRS, and keeps growing to IRS 0.4 in hovering flight condition. As the downwash develops, the region where the lower rotor is affected by the downwash of the upper rotor increases. Furthermore, the downwash strength at the lower rotor increases as well. These make a decrease in the effective angle of attack at the lower rotor. As a result, the thrust coefficient of the lower rotor in hovering flight decrease as IRS gets larger, which is an opposite trend form that in forward flight.

4 Conclusions

Aerodynamic characteristics of two coaxial rotors, Nagashima rotor in hovering flight and Harrington rotor 1 in forward flight, are compared by three different IRS. Vortex structure of the Nagashima rotor is not affected much by the change of IRS, whereas BVI of the Harrington
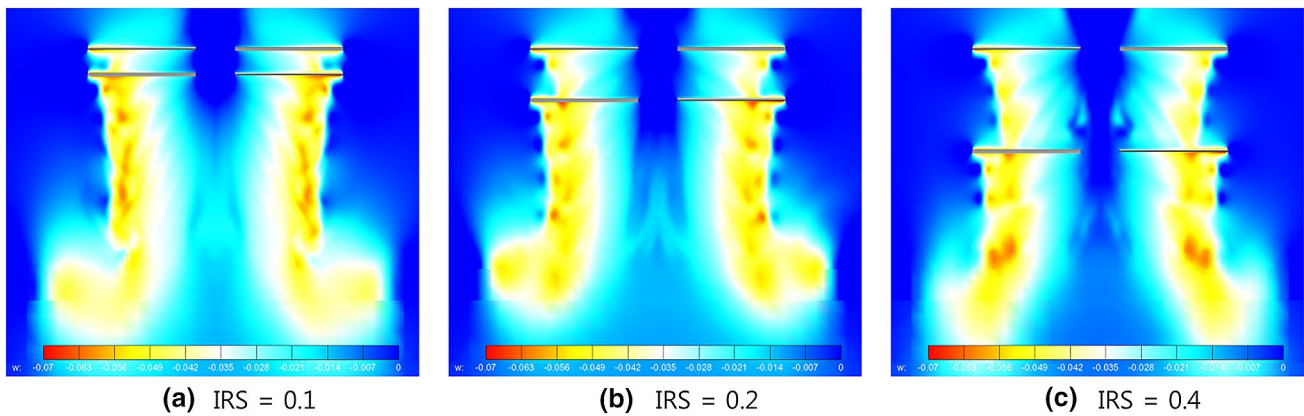
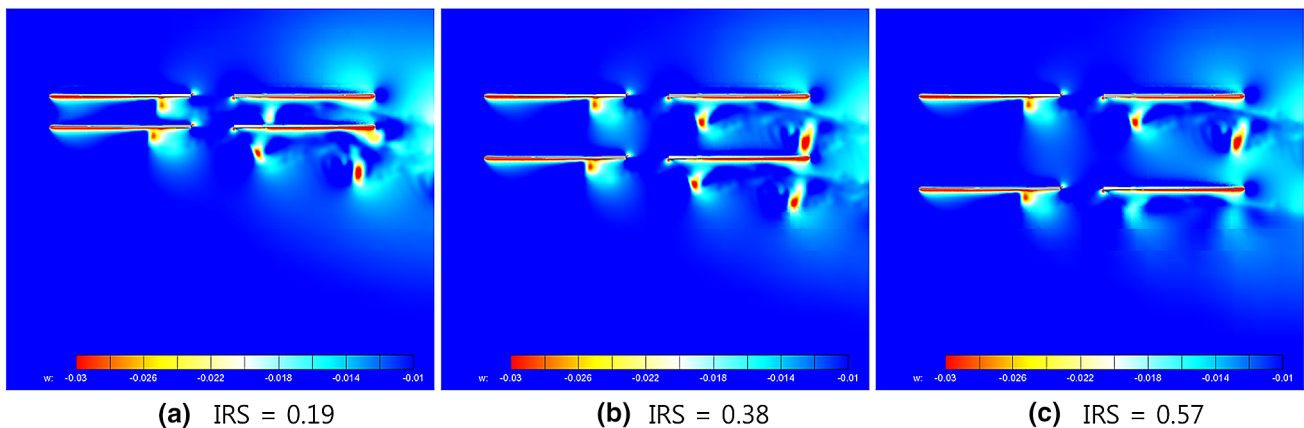**Fig. 13** Downwash of Nagashima rotor viewed from side

Fig. 14 Downwash of Harrington rotor 1 viewed from side

rotor does. Total thrust coefficient of the Nagashima rotor decreases as IRS gets larger. On the other hand, total thrust coefficient of the Harrington rotor 1 increases with larger IRS. The main difference of two rotors in different flight condition is resulted from the opposite trend of the lower rotor thrust coefficient. This difference is found out to be main caused by the undeveloped downwash of the upper rotor in hovering flight with small IRS. The trend of the torque coefficients by IRS is found similar compared to the trend of the thrust coefficients.

The flight condition considered in the present study covers only low-speed rotorcrafts. As a result, the aerodynamic characteristics of the coaxial rotor in high-speed flight condition are needed to be investigated for the actual design of the coaxial rotor.

References

1. Rober DH (1951) Full-Scale-Tunnel Investigation of the Static-Thrust Performance of a Coaxial Helicopter Rotor, NASA TN 2318
2. Nagashima T, Nakanishi K (1978) Optimum performance and load sharing of coaxial rotor in Hover. J Jpn Soc Aeronaut Space Sci 26(293):325–333
3. Manikandan R (2013) Hover performance measurements toward understanding aerodynamic interference in coaxial, tandem, and tilt rotors. In: American Helicopter Society 69th Annual Forum Proceedings, Phoenix, AZ
4. Seokkwan Y, William MC, Thomas HP (2017) Computations of torque-balanced coaxial rotor flows. In: 55th AIAA Aerospace Sciences Meeting proceedings, Texas, Grapevine
5. Griffiths DA, Ananthan S, Leishman JG (2005) Predictions of rotor performance in ground effect using a free-vortex wake model. J Am Helicopter Soc 50(4):302–314
6. Jung MS, Kwon OJ (2007) A parallel unstructured hybrid overset mesh technique for unsteady viscous flow simulations. In: International conference on parallel computational fluid dynamics, ParCFD Paper 2007–024

7. Nakahashi K, Togashi F, Sharov D (2000) Intergrid-boundary definition method for overset unstructured grid approach. AIAA J 38(11):2077–2084
8. Natasha B (2016) Coaxial rotor flow phenomena in forward flight. In: SAE Technical Paper 2016–01–2009
9. Roe PL (1981) Approximate Riemann solvers, parameter vectors and difference scheme. J Comput Phys 43(2):357–372
10. Shur ML, Strelets MK, Travin AK, Spalart PR (2000) Turbulence modeling in rotating and curved channels: assessing the Spalart-Shur correction. AIAA J 38(5):784–792
11. Venkatakrishnan V (1995) Convergence to steady state solutions of the Euler equations on unstructured grids with limiter. J Comput Phys 118(1):120–130
12. Karypis G, Kumar V (1998) Multilevel k-way partitioning schemes for irregular graphs. J Parallel Distrib Comput 48(1):96–129
13. M. J. Aftosmis (1997) Solution adaptive cartesian grid methods for aerodynamic flows with complex geometries. In: Von Karman Institute for Fluid Dynamics, 1997, Lecture Series
14. Jang S, Morris P (2006) Multidimensional interpolation for high order schemes in adaptive grids. J Comput Fluids Eng 11(4):39–47